Accumulation and Continuous Removal of Impurities in Fuel Cells:

I. One-Dimensional Model

R. W. LYCZKOWSKI and DIMITRI GIDASPOW

Institute of Gas Technology, Chicago, Illinois

A mode of operation and a design technique have been developed which permit the attainment of continuous purging of impurities directly from the gas compartments of a fuel cell—either anode, cathode, or both—with the realization of minimum reactant loss, most stable voltage and current output, and operating conditions with respect to reactant gas flow and electrolyte inventory. We have found a way to eliminate the complex periodic purge valves and attendant electronics by a fuel cell system which is both simple in structure and operation and which has a high degree of reliability. The technique was suggested by the observation that in dead-ended fuel cell gas compartments, the inert impurities present in reactant gases tend to accumulate at the dead-ended portion of the cell. Hence a small amount of bleed should be placed there. This observation has been made analytically by solving numerically a system of two partial differential equations simultaneously.

When hydrogen and oxygen or similarly pure reactants are used as fuel and oxidant and where the product of reaction is a condensable gas such as water vapor, it is common practice to make either the anode gas chamber or cathode gas chamber dead-ended. Such designs have been used recently, for example, on the oxygen or cathode chamber of the Apollo (*1*) fuel cell and for both the oxygen and hydrogen chamber of the matrix-type (*2*) fuel cell which may be used in the U.S. Air Force's manned orbiting laboratory (MOL) fuel cell.

Even though the hydrogen and oxygen used in these fuel cells are of high purity, there are, nevertheless, some impurities present in these reactants. These impurities are in the form of noncondensable gases, such as nitrogen, helium, or argon or similar such gases. During the course of operation of these dead-ended cells, the fuel and oxidant are continuously consumed and converted into water, which is then removed from the cell in some fashion. In the case of the above-mentioned Apollo fuel cell, the product water is removed by recirculation of the hydrogen gas through a water condensor. In the case of the MOL fuel cells, the water is removed through a water transport membrane located within the anode chamber of the fuel cell.

When the cell is dead-ended, the noncondensable impurity accumulates, that is, its concentration becomes higher in the gas compartments of the cell. The accumulation of these impurities causes a drop in operating voltage of the cell and a nonuniform current distribution within the cell. Both features are most undesirable. As a result, it is common practice to purge the electrode chambers periodically to allow the impurity to escape from the cell. This periodic purging causes undesirable voltage transients, possible temporary interruption of power, and permanent loss of electrolyte from the cell, as well as other damaging transients, which, it is believed, ultimately lead to total cell failure. Moreover, to accomplish the periodic purging, a complicated set of purge valves and accompanying electronics equipment is required. This equipment adds to the weight of the system without increasing the system's power capability and detracts from overall system reliability. Furthermore, because the impurity is allowed to accumulate between purges, the drop in cell voltage would result in a loss in some efficiency and necessitates a more complex voltage regulation equipment to ensure that a steady voltage level is delivered from the power plant.

In the past, the only attempt to resolve these problems has been by using those systems in which gas recycle, either fuel or oxidant, is employed, and wherein a continuous purge is removed from the recycle loop. This mode of operation eliminates periodic purging and the attendant undesirable transients but adds complexity to the fuel cell system because of the need for gas recycle equipment, and results in lower system efficiency because a substantial portion of reactant is lost during the continuous purge. This paper is directed at the design and operation of an improved fuel cell avoiding the above difficulties.

We have found that it is possible to eliminate the above problems by continuously bleeding gas from the fuel cell electrode chambers themselves. This is possible because it was observed that the inerts always accumulate near the dead-ended portion of the gas compartments. Thus location of a bleed at this point will remove essentially only inerts and only small quantities of reactants if the rate of bleed is slightly greater than the rate of inputs of inerts coming in with the reactants.

MATHEMATICAL MODEL

When a fuel cell is viewed as a chemical reactor producing electricity, it becomes clear that the transport phenomena approach can be used to model an actual fuel cell using differential type polarization data. In constructing our mathematical model, we will assume that our system is one dimensional. One dimensionality may be achieved by distributors, low permeability in the direction of flow (*3*), and use of baffles. The chambers are extremely thin, so the variation of pressure, velocity, and concentration may be neglected in the direction perpendicular to the electrode surface. We will assume that there is a substantial difference between cathode and anode gas purities; thus we need concern ourselves with only one gas chamber at a time. This will usually be the oxygen chamber since hydrogen is generally available in higher purity.

One dimensionality is further bolstered by the fact that Sareen and Gidaspow (*4*) measured the permeability ratio of

an actual Allis-Chalmers (A-C) fuel cell chamber, assuming a porous flow model, and found the ratio to be 8.1 to 1. They calculated an equivalent diameter corresponding closely to the height of a single groove using the permeability measured in the main direction of flow (3). In Part II of this study we will concern ourselves with the two-dimensional aspects of the fuel cell.

Consider a differential element of fuel cell Δx long and h_{av} high (see Figure 1). When the rate of accumulation for reacting species a plus its net outflow by convection is equated to its generation, the species equation becomes, after the usual limiting procedure

$$\left(\frac{h_{av}}{h_{eq}}\right)\frac{\partial X_a}{\partial t}+\frac{\partial(X_a v_a)}{\partial x}=-\frac{I}{h_{eq}nFC} \tag{1}$$

h_{eq} may be estimated by using the additive resistance concept to account for the changes in area which are available for flow.

The total molar concentration C for the ideal gas is constant, since it is known that the absolute pressure in the fuel cell chamber varies little. Extremely small fluctuations in pressure cause the reacting gas to be drawn into the cell upon load demand.

We made the assumption that the water vapor distributes itself uniformly throughout the cell at the equilibrium partial pressure of water vapor over a potassium hydroxide aqueous solution, and therefore its mole fraction is constant. At the typical operating conditions, that is, 194°F. and 36.7 lb./sq. in. abs., the partial pressure of water vapor is 11 mole % or approximately 240 mm. Hg for a 37.5 wt. % aqueous potassium hydroxide solution (2). This assumption holds since the drying effect of the entering gases is confined to a small area near the inlet (5). We may conveniently think of X_a now as the mole fraction of reacting gas plus water vapor. The mole fraction of the inert is then represented by $1 - X_a$. Finally, we assumed that isothermal operation exists.

After we perform another species balance for the inert gas and add it to Equation (1), we obtain the continuity equation

$$\frac{\partial v^*}{\partial x}=-\frac{I}{h_{eq}nFC} \tag{2}$$

The use of the continuity equation together with Fick's first law of diffusion causes Equation (1) to assume the form

$$\left(\frac{h_{av}}{h_{eq}}\right)\frac{\partial X_a}{\partial t}+v^*\frac{\partial X_a}{\partial x}-\frac{X_a I}{h_{eq}nFC}=D_{ab}\frac{\partial^2 X_a}{\partial x^2}-\frac{I}{h_{eq}nFC} \tag{3}$$

The function I, which is a function of X_a and the voltage, must be obtained from experiment. We used a piecewise linear approximation for this relation which was obtained from an actual polarization curve using the Allis-Chalmers data (2). Such polarization curves are obtained in either of two ways: In the first case, the reactant gas with desired amounts of impurity is passed rapidly over an electrode surface at constant pressure while completely pure gas is passed over the other electrode surface. Alternatively, the pressure of pure reactant gas may be changed in one chamber. The important fact is that polarization curves must be generated at different partial pressures of the reacting gas. The data which were obtained by A-C (2) was for the oxygen chamber since high purity hydrogen is more readily available. As already mentioned, the purity of hydrogen is so high, it plays no role in the impurity buildup problem as far as the calculations we obtained are concerned.

The approximation used for I is

$$I = 130. + 20.\,X_a \qquad (0.35 \le X_a \le 1.0) \tag{4}$$

$$I = 77.7 + 169.5\,X_a \qquad (0.153 \le X_a \le 0.35) \tag{5}$$

and

$$I = -265.1088 + 2410.08\,X_a \qquad (0.11 \le X_a \le 0.153) \tag{6}$$

Below $X_a = 0.11$, I is zero.

Equations (4) through (6) represent the piecewise linear fit of the I versus X_a curve which is obtained from the experimental polarization curve as presented in Figure 2. To construct Figure 2 we assumed that there is always a constant external resistance equal to the slope of the polarization curve at the nominal operating point of the cell. For this study, we used a nominal operating point of 150 mamp./sq. cm. at 36.7 lb./sq. in. abs. and 194°F. The slope of the polarization curve there is 6.095 ohm/sq. cm. This resistance is actually the sum of the internal and external resistances, but we assume that since the external resistance is so much larger than the internal resistance, the value is constant.

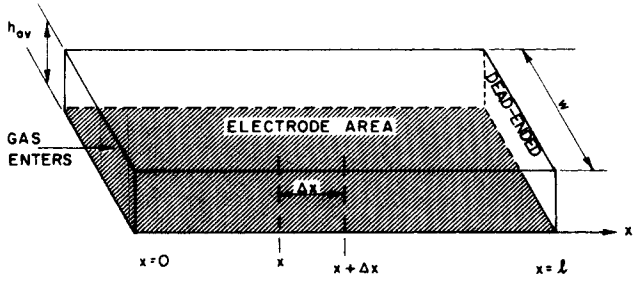

Fig. 1. One-dimensional fuel cell geometry and coordinate system.

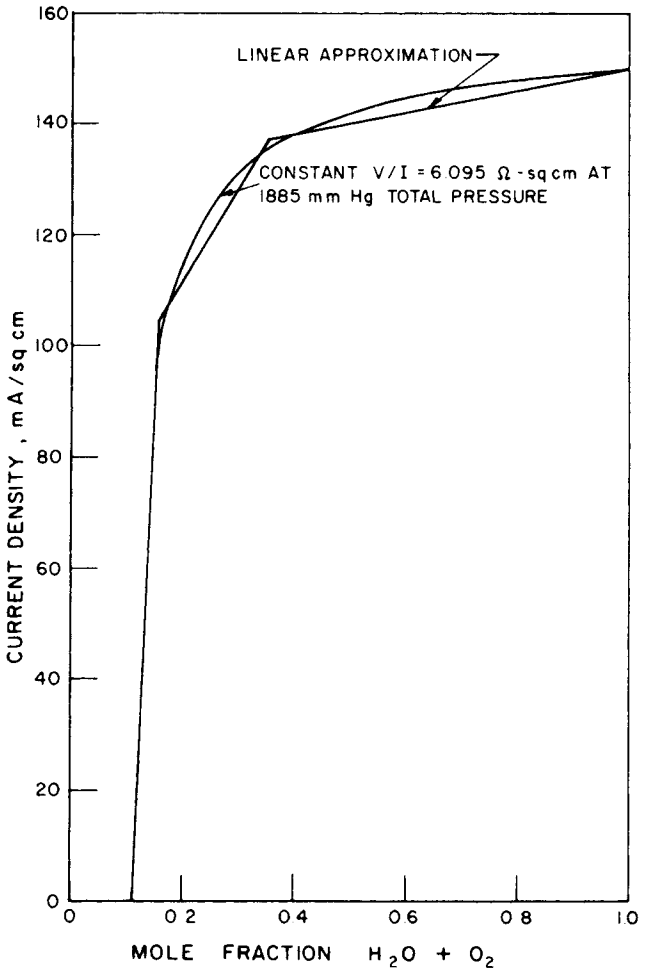

Fig. 2. Current density function at constant external resistance (2).

DIMENSIONLESS EQUATIONS AND BOUNDARY CONDITIONS

It will be convenient now to introduce the dimensionless parameters and variables D^*, $\bar{I}$, $\bar{v}^*$, $\bar{x}$ and θ. Substitution of these definitions into Equations (2) and (3) results in the dimensionless governing equations

Species a:

$$\frac{\partial X_a}{\partial \theta} + \bar{v}^* \frac{\partial X_a}{\partial \bar{x}} - X_a \bar{I} = D^* \frac{\partial^2 X_a}{\partial \bar{x}^2} - \bar{I} \tag{7}$$

Continuity:

$$\frac{\partial \bar{v}^*}{\partial \bar{x}} = -\bar{I} \tag{8}$$

The boundary conditions are that initially the mole fraction of oxygen and water vapor are constant. Gas a with impurity enters with mole fraction X_a^i at $\bar{x} = 0$. At the dead end of the cell, zero gradient exists. Since this boundary condition is not immediately evident, it will now be quickly derived.

Application of Fick's law at $x = \ell$ results in

$$X_a v_a|_\ell - X_a v^*|_\ell = -D_{ab} \left.\frac{\partial X_a}{\partial x}\right|_\ell \tag{9}$$

The species a balance Δx away from $x = \ell$ is

$$\left.\frac{\partial X_a}{\partial t} \Delta x + \frac{h_{eq}}{h_{av}} X_a v_a\right|_{t,\ \ell - x} = -\frac{I \Delta x}{nFCh_{av}} \tag{10}$$

In the limit as $\Delta x \longrightarrow 0$, we obtain $X_a v_a|_\ell = 0$. This means that physically no material is leaving the system through the dead end. A similar balance and limiting procedure for the inert gas b yields the fact that $v^*|_\ell = 0$ and hence the gradient of X_a is zero as seen from Equation (9).

The final condition is the setting of the amount of bleed. These conditions are stated mathematically now and collected for reference.

$$X_a(0, \bar{x}) = X_a^0 \tag{11}$$

$$X_a(\theta, 0) = X_a^i \tag{12}$$

$$\frac{\partial X_a(\theta, 1)}{\partial \bar{x}} = 0 \tag{13}$$

and finally, upon integration of Equation (8) for any time θ

$$\bar{v}^*(\theta, \bar{x}) = \int_{\bar{x}}^{1} \bar{I}\, d\bar{x} + \bar{v}^*(\theta, 1) \tag{14}$$

During the dead-ended operation of the fuel cell, $\bar{v}^*(\theta, 1) = 0$ and during the continuous bleed, its value must be assigned. It is not necessary to begin a cell with uniform concentration of reacting gas, since an arbitrary distribution is as easily handled in the model as is the uniform case.

During zero bleed operation, Equation (13) implies that no material leaves the fuel cell chamber at $\bar{x} = 1$. During bleed operation, we still have via Fick's law Equation (9). However, since all material now leaves by bulk motion alone, $X_a v_a|_\ell = X_a v^*|_\ell$ and so the gradient remains zero.

Parameters used in the calculations include the electrode area (0.1904 sq. ft.), the fuel cell length (0.5618 ft.), the one-dimensional chamber height (0.00406 ft.), and the binary diffusion coefficient of oxygen-argon (0.61 sq. ft./hr.) (6). The chamber height used assumes that $h_{eq} = h_{av}$ = the height of a single slot.

Previous work which addressed itself to a similar problem was performed by A-C (2). In contrast to the model we have presented, they assumed that there were N well-stirred reactors in series. They wrote a species balance for each reactor and then solved the N resulting simultaneous ordinary differential equations. In the limit, as the number of well-stirred reactors approaches infinity, their model should approach ours.

SOLUTION BY FINITE DIFFERENCES

Equation (7) is converted to finite-difference form by using a three-point Taylor series expansion in the space coordinate and a two-point expansion in the time coordinate. The completely explicit molecule assumes the following form after the coefficients of $X_a(I, J)$, $X_a(I, J + 1)$, and $X_a(I, J - 1)$ are collected:

$$X_a(I + 1, J) = X_a(I, J)\,[\Delta\theta \bar{I}(I, J) - 2RD^* + 1] + X_a(I, J - 1)\left[\frac{\Delta\theta}{2\Delta\bar{x}} \bar{v}^*(I, J) + RD^*\right] + X_a(I, J + 1)\left[RD^* - \frac{\Delta\theta}{2\Delta\bar{x}} \bar{v}^*(I, J)\right] - \Delta\theta \bar{I}(I, J) \tag{15}$$

where $X_a(I + 1, J) \equiv X_a(\theta + \Delta\theta, x)$ and $X_a(I, J \pm 1) \equiv X_a(\theta, \bar{x} \pm \Delta\bar{x})$. If the sufficient stability conditions of Keller (7) are applied to Equation (15) by utilizing the linear approximation for $\bar{I}$, we obtain the following restrictions:

$$\Delta\bar{x} \leq \frac{2D^*}{|-\bar{v}^*(\bar{x})|} \tag{16}$$

and

$$R = \frac{\Delta\theta}{\Delta\bar{x}^2} \leq \frac{1}{2D^* - \Delta\bar{x}^2(\bar{I} - A')} \tag{17}$$

where A' is the maximum slope of the linear approximations for $\bar{I}$.

The maximum value of $|-\bar{v}^*(\theta, \bar{x})|$ occurs at zero time and equals $1 + \bar{v}^*(0, 1)$; therefore we will require that

$$\Delta x \leq \frac{2D^*}{1 + \bar{v}^*(0, 1)} \tag{18}$$

The maximum value of $2D^* - \Delta\bar{x}^2(\bar{I} - A')$ is $2D^* + \Delta\bar{x}^2 A'$ so that Equation (17) becomes

$$R \leq \frac{1}{2D^* + \Delta\bar{x}^2 A'} \tag{19}$$

The value of D^* was estimated by calculating the diffusivity for oxygen and argon using reference 6. D_{ab} calculated from that reference is 0.61 sq. ft./hr. at a pressure of 2.5 atm. and a temperature of 90°C. This makes D^* approximately 0.0144 at an initial average current density of 150 mamp./sq. cm. for dead-ended operation.

Therefore $\Delta x \leq 0.0288/[1 + \bar{v}^*(0, 1)]$. Using the largest value of A', $R \leq 25.8$ for dead-ended operation and slightly less for bleed operations.

The initial condition to be used is $X_a(0, J) = X_a^i$ for $J = 2$ to $J = N$, where $N = 1/\Delta x + 1$. The boundary condition at $\bar{x} = 0$ is $X_a(I, 1) = X_a^0$. At $\bar{x} = 1$, zero gradient exists. This boundary condition may be approximated in finite-difference form a number of ways. If $X_a(I, N + 1)$ is set equal to $X_a(I, N - 1)$ in Equation (15) used at the boundary ($J = N$), the boundary molecule becomes

$$X_a(I + 1, N) = \Delta\theta \bar{I}(I, N)\,[X_a(I, N) - 1] + 2RD^*\,[X_a(I, N - 1) - X_a(I, N)] + X_a(I, N) \tag{20}$$

To obtain Equation (20), the governing species equation [Equation (7)] is assumed to hold at the boundary.

Another possibility is to write an implicit off-center molecule for the zero derivative, but use it completely explicitly because all the interior points have been already calculated using Equation (15). This approximation is

$$X_a(I + 1, N) = \tfrac{4}{3} X_a(I + 1, N - 1) - \tfrac{1}{3} X_a(I + 1, N - 2) \tag{21}$$

Numerical calculations using Equation (21) agreed closely with those using Equation (20), but all results reported herein have been calculated using Equation (20). A grid size check for dead-ended operation was performed using a fixed value of $R = 25$ and values of $\Delta\bar{x} = 0.025$, 0.02, and 0.01667. This study revealed that $\Delta\bar{x} = 0.025$ is sufficiently accurate not to warrant a finer grid. Results were changing in the third to fifth decimal place. Even when the restriction of Equation (18) was violated by using $\Delta\bar{x} = 0.0333$, results were accurate up to $\theta = 100$, for dead-ended operation, at which point the calculations became unstable.

In order to estimate what effect diffusion has on dead-ended operation, we set up a computational molecule for the case of zero diffusion. Using the Euler two-point expansion for the space derivative and combining the integrated form of the continuity equation, Equation (14), we obtained

$$X_a(I+1, J) = X_a(I, J)\left[1 - \int_{(J-1)\Delta x}^{1} \bar{I}\, d\bar{x}\, \frac{\Delta\theta}{\Delta\bar{x}} + \bar{I}(I, J)\,\Delta\theta\right] + X_a(I, J-1) \int_{(J-1)\Delta\bar{x}}^{1} \bar{I}\, d\bar{x}\, \frac{\Delta\theta}{\Delta\bar{x}} - \bar{I}(I, J)\,\Delta\theta \quad (22)$$

No boundary condition is needed for the species equation at $\bar{x} = 1$. From the method of characteristics, stability requires that $\Delta\theta \leq \Delta\bar{x}\,\bar{v}^*$. The maximum value of $\bar{v}^*$ is 1, so that for convenience, we require $\Delta\theta \leq \Delta\bar{x}$ for stability. We decreased $\Delta\bar{x}$ to as small a value as possible and then extrapolated the results to zero grid size. In all calculations we set $\Delta\theta = \Delta\bar{x}$.

To obtain the velocity profile at any time, a quadrature subroutine was used which evaluated the integral in Equation (14) with a maximum error of $(\Delta\bar{x})^3$ and a minimum error of $(\Delta\bar{x})^5$. This integration was performed after the concentration and current density had been calculated.

DEAD-ENDED OPERATION

For dead-ended operation, we assumed that 0.5% of inert argon enters with the oxygen so that we could directly compare our results for average current density to those obtained by A-C (2).

Figure 3 presents typical dead-ended concentration distributions as a function of time and spatial coordinates. The value of $R = 25$ and $\Delta\bar{x} = 0.025$. The computation time required for a real time of 67 min. was approximately 10 hr. on the Institute of Gas Technology's small IBM 1800 computer using extended precision arithmetic. This corresponds to approximately 1 min. on a Univac 1108. In the figure we can see a series of s-shaped curves. They represent the concentration (mole fraction) of oxygen and inert impurity for different times as a function of fuel cell length. A point on any one of the curves for a fixed value of θ, the dimensionless time, gives the value of the sum of the mole fraction of equilibrium water vapor and oxygen. The difference is made up of the inert which entered with the oxygen. The 0.5% amount of impurity (assumed to be argon) is represented in the figure by a point at $\bar{x} = 0$ and $X_a = 0.995$ (extreme left) at the inlet port. X_{H_2O} represents the constant equilibrium mole fraction of water vapor over a 37.5 wt. % potassium hydroxide solution at a total pressure of 36.7 lb./sq. in. abs. and a temperature of 194°F.

The figure shows that the inert accumulates at the dead-ended portion of the cell, represented in the figure at $\bar{x} = 1.0$. Even though only 0.5% of impurity entered with the oxygen, after even a short time this percentage becomes quite a bit larger than this at the dead end. This same behavior was found to occur in the more realistic two-dimensional model which utilizes Darcy's law. As time goes on, the inert, in effect, begins to blanket the electrode, resulting in a drop of cell current and voltage efficiencies. What is presently done in practice is to open the dead end periodically to a reduced pressure, causing the inerts to be sucked out of the chamber. This purge, as it is called, causes the pressure in the cavity to drop, forcing in much more rapidly, fresh, purer, inlet fuel. This purging operation results in a restoration of the performance level. As soon as the valve to the lower pressure is closed, the entrance of purer fuel decreases to the prepurge level, and inerts begin to accumulate once again. Almost inevitably, the voltage efficiency drops momentarily to a lower level during the purge. The reason for this drop is not fully understood but may be caused in part by partial drying out of the electrode or temperature fluctuations.

Curves similar to those found in Figure 3 have been obtained previously by Allis-Chalmers (2). Average current efficiency as a function of time obtained from the theoretical calculations for dead-ended operation was in reasonable agreement with experimental results obtained from their test cell as shown by Figure 4, where there is also a comparison to a simple well-stirred tank model.

The well-stirred model agrees more closely with their experimental results than their model does for shorter times. After the beginning of the third time period, the well-stirred model decays much too rapidly. This too-rapid decay may be explained by the fact that all of the fuel cell is never operating in the regime where the current density is decreasing as rapidly as Equation (6) indicates. In fact, near the fuel entrance port, X_a is always near 0.995 for all times of interest. This shows the defect of the well-stirred reactor approach and indicates that consideration of the fluid mechanics in the cavity yields a closer agreement between theory and experiment.

It should be emphasized that Figure 3 is merely typical of those that might be generated because we used just one

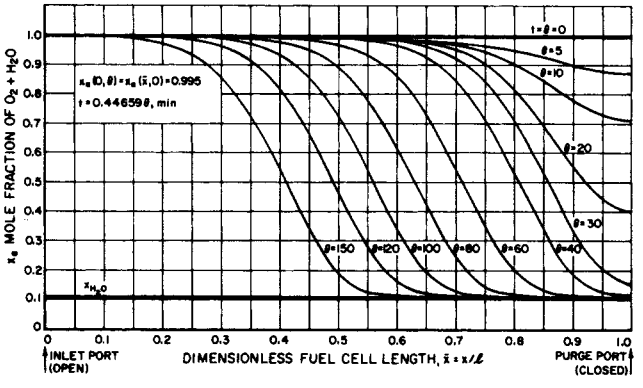

Fig. 3. Inert buildup in a conventional dead-ended fuel cell.

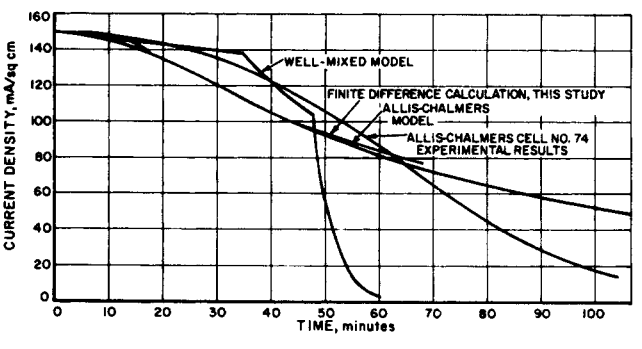

Fig. 4. Comparison of average current densities from well-stirred and one-dimensional models with Allis-Chalmer's results; 0.5% impurity.

special polarization curve in the calculations. The model may incorporate any general functional dependence of current density upon reactant gas concentrations. The resulting concentration profiles will still look the same, however. The entering gas purity may, in addition, be varied arbitrarily, and may even be taken to be a function of time.

Figure 5 represents the velocity distribution associated with the one-dimensional dead-ended fuel cell operation. At zero time the velocity decreases linearly with distance along the fuel cell electrode because the initial current density is uniform due to the homogeneous initial distribution of inerts. As time progresses, the linear character of the velocity is preserved at the entrance of the fuel cell and merely lies below that for zero time. Eventually the figure shows that the portion of the cell near the dead end becomes motionless as the current density falls due to inert accumulation.

We assessed the effect of neglecting molecular diffusion entirely for dead-ended operation. To obtain results, we employed the same piecewise linear approximation for $\bar{I}$ as before, with the same initial and boundary conditions on X_a. Figure 6 is a plot of the local concentration of water vapor and oxygen. The most pronounced difference between this plot and that obtained in Figure 3 is the much steeper slope of the curves. Also totally lacking is the s-shaped character found previously. These curves exhibit a frontlike buildup of inerts. The velocity profiles associated with the zero diffusion model are found in Figure 7. The plots reveal absolutely straight lines which contrast with the slight curvature of the velocity curves found in Figure 5 for the diffusion model.

Figure 8 compares the average current density as a function of time with and without diffusion. The conclusion which can be drawn from the calculations is that in dead-ended operation, diffusion cannot be dropped in the model. When diffusion is neglected, the average current density drops much faster than with diffusion, and consequently the average current density agrees even less with the experimental results.

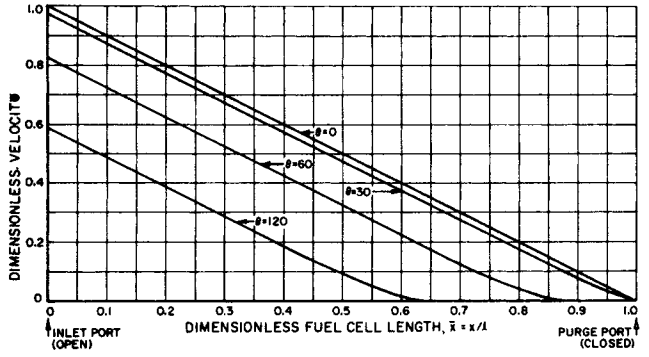

Fig. 5. Velocity profile for the one-dimensional model with $D^* = 0.01438$; 0.5% impurity; dead-ended operation.

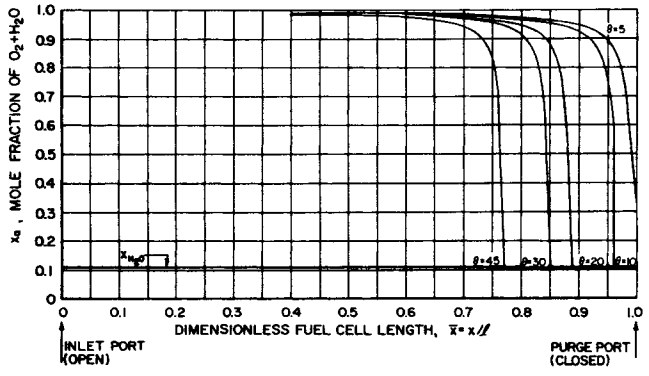

Fig. 6. Variation in local concentrations of water vapor and and oxygen with time; dead-ended operation; $D^* = 0$; 0.5% impurity.

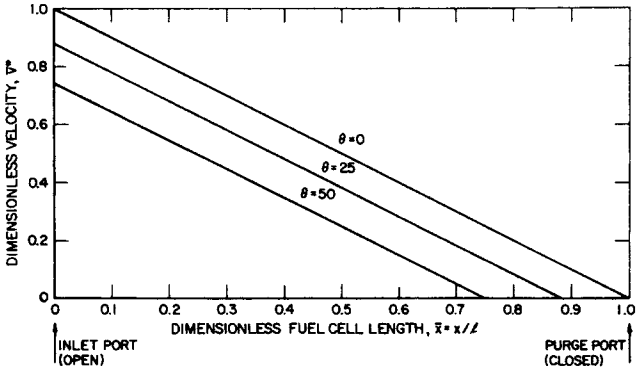

Fig. 7. Variation of velocity profiles with time; dead-ended operation; 0.5% impurity.

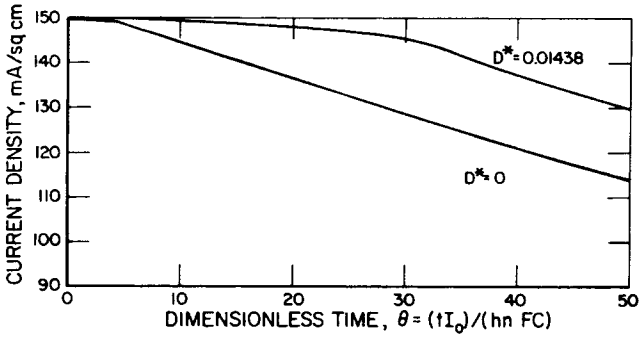

Fig. 8. Comparison of average current density with and without diffusion; dead-ended operation; 0.5% impurity.

CONTINUOUS BLEED OPERATION

Inspection of the concentration curves for the dead-ended operation showed that the impurity accumulated near the dead-ended side of the cell. This led us to suspect that a small bleed at this position will result in the removal of impurities from the cell. Discussion of this concept with the hardware manufacturer and the government sponsors showed that this was a novel concept and could be made practical. The rate of bleed must be set slightly above the rate of introduction of impurities into the cell. A small coil connected to the dead-ended side of the cell can replace the present valve system.

For the continuous bleed studies, we chose a 1% inert impurity to show that with even a more impure fuel, continuous bleed will allow reasonable operating levels. Figure 9 represents the steady state concentration distribution curves when different amounts of bleed are introduced at the dead end of the cell chamber. The bleed is placed there, since from Figure 3 it is obvious that this is where the inerts are accumulating. What we now see illustrated in Figure 9 is not a continual increase of the inerts, but rather a buildup to a steady state which is dependent on the bleed rate. The higher the bleed rate, the more the cell becomes throughflow and the faster it reaches a steady state. Inert buildup decreases as well. The value of the mole fraction at $\bar{x} = 1$ will tell how pure the exiting gas is. The higher the bleed, the purer is the leaving gas. In addition, we may also calculate the rate of pure reactant gas leaving.

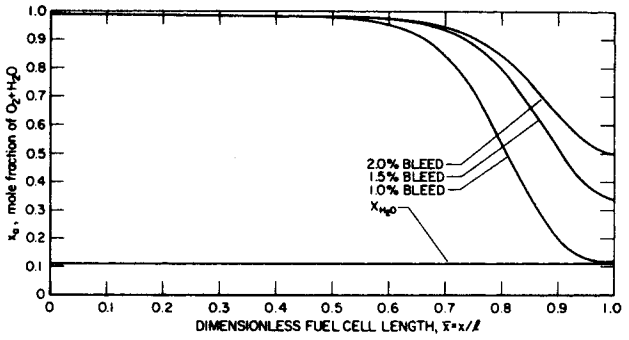

Fig. 9. Steady state concentration distributions with bleed; 1% impurity.

Figure 10 shows the average current density as a function of time for dead-ended and continuous bleed operations. With no bleed, the current efficiency rapidly falls to low values as does the voltage efficiency (Figure 10). With a small amount of bleed, an acceptable current density is reached with no further decrease as time goes on. Thus with hardly any loss of cell efficiency, an acceptable performance level is achieved without the necessity of ever purging the cell. As a further bonus, the ultrahigh purity gases which are presently being used may be replaced with the normal purity fuels which are used for the liquid hydrogen-liquid oxygen rockets.

Figure 11 shows that optimum fuel utilization efficiency occurs at a bleed rate which is just slightly higher than the percent impurity. The bleed rate used in the calculations is defined to be a certain constant percentage of the nominal operating point consumption rate, in this case 150 mamp./sq. cm. The steady state current drop below the initial average current density decreases with increasing bleed. But, because the exiting gas is more pure with respect to oxygen, more oxygen is leaving. If this wasted oxygen were to be converted into current, it would increase with the bleed rate. The intersection of the two curves yields the maximum fuel utilization and tells how much current is being wasted. In actual operation the bleed rate will be determined by the maximum load, since this corresponds to the highest rate of introduction of impurities. This will allow operation without any necessity for intermittent purge. With the pure gases normally employed, the waste of fuel is very small.

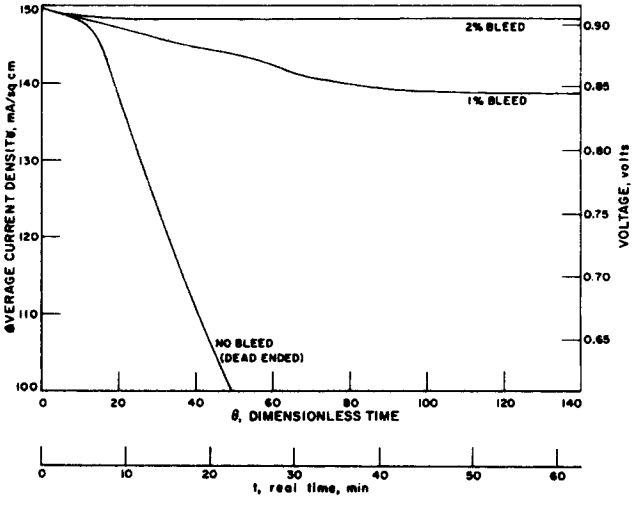

Fig. 10. Average current density and voltage for various bleed rates; 99% pure oxygen feed.

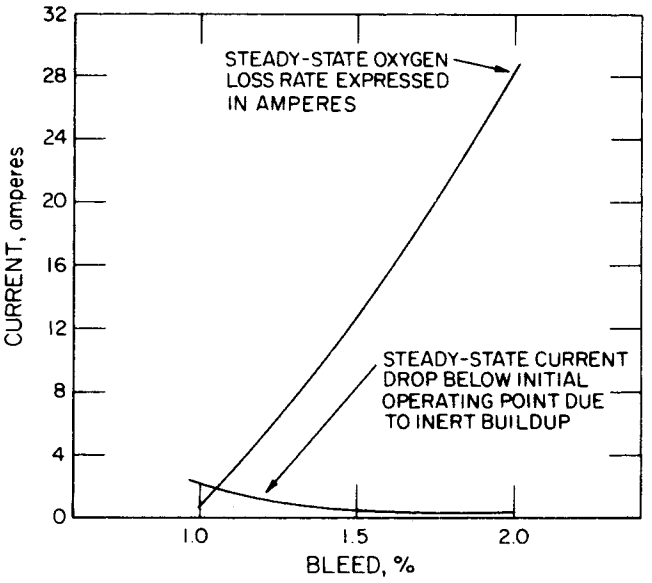

Fig. 11. Optimization of fuel utilization; 1% impurity.

RECOMMENDATION

Based upon our solution of governing partial differential equations, we recommend that the present complex purge system be replaced by a continuous bleed coil connected to the far end of each fuel cell compartment.

ACKNOWLEDGMENT

This study was supported by the National Aeronautics and Space Administration under Contract No. NAS8-21159. The authors are grateful to Richard Boehme of the NASA Marshall Space Flight Center for suggesting this problem. They also thank B. S. Baker, D. Y. C. Ng, and C. W. Solbrig for their various services, without which this work could not have been carried out.

NOTATION

A_{eq} = equivalent area available to flow, sq. ft.
a = reacting species
b = inert species
C = total molar concentration, lb.-moles/cu. ft.
D^* = dimensionless diffusion coefficient, $= D_{ab}h_{eq}nFC/\ell^2 I_0$
D_{ab} = binary diffusion coefficient of reacting gas a in inert gas b, sq. ft./hr.
F = Faraday's constant, 12,158 (amp.)(hr.)/lb.-equiv.
h_{av} = height of fuel cell channel $= V/S$, ft.
h_{eq} = $A_{eq}\ell/S$, equivalent height available to flow
I = current density, amp./sq. ft.
I_0 = average current density at zero time, amp./sq. ft.
$\bar{I}$ = I/I_0
ℓ = length of the fuel cell chamber, ft.
n = number of lb.-equiv. per lb.-mole of oxygen (=4)
N = $1/\Delta\bar{x} + 1$
S = electrode area, $= \ell \cdot w$, sq. ft.
t = time, hr.
V = actual cell volume, $= h_{av}\, w \cdot \ell$, cu. ft.
v^* = molar average velocity, ft./hr.
$\bar{v}^*$ = dimensionless average velocity, $= v^* \Big/ \left(\dfrac{I_0}{h_{eq}nFC}\right)$
w = cell width, ft.
x = space coordinate, ft.
$\bar{x}$ = dimensionless space coordinate, x/ℓ
X_a = mole fraction of reacting gas
X_a^i = mole fraction of reacting gas at zero time

X^0_a = mole fraction of reacting gas at $\bar{x} = 0$
$X_a(I + 1, J \pm 1) = X_a(\theta + \Delta\theta, \bar{x} \pm \Delta\bar{x})$
θ = dimensionless time, $= tI_0/(h_{av}nFC)$

LITERATURE CITED

1. Jones, J. C., and J. E. Cox, *Energy Conversion*, **8**, 113–115 (1968).
2. Allis-Chalmers Res. Div., "Summary Report," *Contract No. NAS8-5392* for George C. Marshall Space Flight Center, NASA Huntsville, Ala., Milwaukee (NAS8-5392-SR-0001) (Jan. 15, 1966).
3. Gidaspow, Dimitri, and S. S. Sareen, *AIChE J.*, **16**, 560–568, (1969).
4. Inst. Gas Technol., *Fifth Quart. Rept. Contract No. NAS8-21159* for George C. Marshall Space Flight Center, NASA, Huntsville, Ala., Chicago (NAS8-21159-QPR-005) (Dec. 1968).
5. ———, *Sixth Quart. Rept.* (NAS8-21159-QPR-006) (Mar. 1959).
6. Fuller, E. N., P. D. Schettler, and J. C. Giddings, *Ind. Eng. Chem.*, **58**, 19–27 (May 1966).
7. Keller, H. B., in "Mathematical Methods for Digital Computers," A. Ralston and H. S. Wilfe, eds., Chap. 12, Wiley, New York (1960).

Manuscript received June 30, 1969; revision received October 14, 1969; paper accepted October 20, 1969. Paper presented at AIChE Washington meeting.

Pressure Drop and Holdup in Horizontal Slug Flow

E. J. GRESKOVICH and A. L. SHRIER

Esso Research and Engineering Company, Florham Park, New Jersey

The Dukler-Hubbard slug-flow model is used along with independent correlations for in situ holdup and slug frequency to predict pressure drops for two-phase slug flow. The holdup and frequency correlations are for the most part based on data for air-water flowing in a 1.50-in. pipe. Predictions of pressure drop using this approach are compared with experimental data taken from studies utilizing various systems and pipes from 1.50 to 6.065 in. in diameter. Alternative correlations by Dukler and Hughmark for predicting two-phase pressure drops and holdup, respectively, are included for comparison. In general, the present approach is at least equivalent to the Dukler-Hughmark method, and for values of $\Delta P/L > 0.06$ lb./sq. in./ft. appears to be slightly better.

The simultaneous flow of gas and liquid in pipes is frequently encountered in refineries, chemical plants, and pipelines. For designing these systems, reliable techniques are needed for predicting liquid holdup and pressure drop for gas-liquid flows under various conditions. This paper concerns the prediction of holdup and pressure drop for one of the more common and important situations—two-phase slug flow in horizontal pipes.

Early two-phase flow studies emphasized the development of overall pressure drop and holdup correlations encompassing all types of flow regimes. Furthermore, most of the experimental data were obtained from relatively small and short pipes. Lockhart and Martinelli (*13*) developed one of the first general correlations. Although various other general correlations have since been proposed, the original Lockhart-Martinelli approach is still in many respects the best, as discussed by Dukler et al. (*4*); however, expected errors in predicted pressure drops are on the order of ±30% or more. The general correlation procedures yield fair predictions of pressure drop for all flow regimes because they are based on a large amount of correlatable data. However, when these correlations are applied to systems other than those used in their development, or to flow over extended distances (definitely established flow), predicted pressure drops can be in error by as much as a factor of 2. For more reliable predictions of pressure drop, correlations based on specific models for individual flow regimes are preferable.

More recently, a number of frictional pressure drop correlations have been developed through similarity analysis by Dukler et al. (*4, 5*). A comparison of pressure-drop predictions with a large number of data points showed that case II, based on a model that assumed homogenous flow with slip between the phases, was superior to all other cases as well as to other pressure-drop correlations tested. This correlation is the most reliable published general correlation for predicting frictional pressure drop (*1*). In order to use the Dukler et al. correlation, an accurate estimation of in situ holdup is necessary. Dukler et al. (*4*) tested several available holdup correlations with a substantial number of data points and concluded that the Hughmark correlation (*11*) was clearly the best. Therefore the Hughmark holdup correlation combined with the Dukler et al. equation (case II) represents the best general pressure-drop prediction method available [see sample calculation by Anderson and Russell (*1*)]. This combination will be referred to hereafter as the Dukler-Hughmark method.

This paper describes an alternative to the Dukler-Hughmark method for the particular case of horizontal slug flow. The present approach utilizes a slug-flow model developed by Hubbard and Dukler (*10*), a holdup correlation

E. J. Greskovich is at Bucknell University, Lewisburg, Pennsylvania.